Efficient photothermal catalytic oxidation of toluene by $La_{1-x}Fe_xMnO_3$ with full spectrum response: The effects of Fe doping and photoactivation

Qi Yu [a,b], Caiting Li [a,b,*], Jungang Zhao [a,b], Xuan Liu [a,b], Le Huang [a,b], Youcai Zhu [a,b], Kuang Yang [a,b], Ziang Zhang [a,b], Dengsheng Ma [a,b], Ying Zhang [a,b], Qi Huang [a,b]

[a] College of Environmental Science and Engineering, Hunan University, Changsha 410082, PR China
[b] Key Laboratory of Environmental Biology and Pollution Control (Hunan University), Ministry of Education, Changsha 410082, PR China

ARTICLE INFO

Keywords:
Photothermal catalysis
Fe doping
Photoactivation
Reactive oxygen species
Toluene oxidation

ABSTRACT

Developing efficient photothermal catalysts with full spectrum response is one of the frontier topics in photothermal catalytic of VOCs. In this work, $La_{1-x}Fe_xMnO_3$ ($0 \leq x \leq 0.2$) was synthesized via citrate sol-gel method. Under full spectrum illumination of 1.3×10^4 W/m², $La_{0.9}Fe_{0.1}MnO_3$ exhibited a more superior activity (86.7% toluene conversion and 84.6% CO_2 yield). Through controlled experiments, not only the origin of photothermal activity, but the possible intrinsic drivers (Fe doping and photoactivation) of the enhanced activity were also revealed. Particularly, the mechanistic details of their facilitating reactions were thoroughly studied, where the improved mobility and activation of lattice oxygen played the primary role. Moreover, the co-effect of Fe doping and photoactivation on the resistance to complex gas components (SO_2, H_2O) and durability was systematically investigated. Eventually, the plausible pathways and mechanisms of toluene oxidation were proposed. This study provides a new insight into photothermal catalysts with full spectrum response for environmental remediation.

1. Introduction

In recent years, some hazardous volatile organic compounds (VOCs) have attracted growing attention (e.g., formaldehyde, benzene, toluene, and acetone) due to their carcinogenic and teratogenic properties [1], as well as being important precursors of ozone, particulate matter, and photochemical smog, which adversely affect human health and ecological environment [2]. Many end-of-pipe methods have been applied to eliminate VOCs, such as absorption [3], plasma decomposition [4], and photo/thermal catalytic oxidation [5,6]. At present, photo/thermal catalytic oxidation (PCO/TCO) is the dominant technology to degrade VOCs into harmless products [7,8]. However, PCO is usually limited by the low efficiency of light-utilization, while TCO requires high energy consumption, which hinders their further development [9]. Photothermal catalytic oxidation (PTCO) provides a novel strategy to stimulate the synergy between PCO and TCO, which is currently one of the frontier research topics for VOCs degradation [10,11]. It perfectly combines the high catalytic efficiency and stability of TCO with the low energy consumption of PCO, and with this approach, the ultraviolet (UV), visible (VIS), and infrared (IR) light in solar light can be exploited more effectively [12]. In other words, PTCO provides a more efficient

conversion of solar (especially for low-energy photons) to chemical energy, which is of great significance for solving energy and environmental problems. Moreover, light has been shown to have an activating effect on the surface oxygen species, which can significantly optimize the reaction path [13]. PTCO technology is also found to promote water resistance and coke resistance while simultaneously enhancing catalytic activity [14,15]. Therefore, PTCO is expected to be effective in restraining the deactivation of catalyst, which makes it promising for practical complex flue gas applications, especially in industrial painting, steel plants, and petrochemical industries [5].

Since the majority of the energy required for PTCO reaction is derived from light-to-heat conversion [16], the broad light wavelength absorption (covering IR range) and efficient photothermal conversion (coupling the captured photons into thermal energy) are prerequisites for an ideal photothermal catalyst. Recent studies have confirmed that ABO_3-type perovskite oxides may be one of the promising photothermal catalyst candidates [17,18]. Thereinto, $LaMnO_3$-based materials receive much focus in photothermal catalysis of VOCs due to their great reducibility and surface oxygen availability. As reported by Chen et al. [19], $LaMnO_3$ showed great catalytic activity for gaseous styrene under VIS illumination, and Li et al. [17] demonstrated that toluene could be

---

efficiently oxidized on $CeO_2/LaMnO_3$ under IR illumination. In general, VIS–IR light with low photon energy has a limited ability to excite the traditional PCO, but it exhibits a significant heating effect, thus driving the redox reactions [20]. Additionally, it had been reported that the light in the high-energy UV region could excite photogenerated carriers over $LaMnO_3$-based materials, and further actuated the PCO reaction [21]. If the high-energy UV region and VIS-IR region are combined to couple the optical and thermal effects, $LaMnO_3$-based materials will show a more distinctive PTCO performance. Nevertheless, it has not been systematically investigated so far.

On the other hand, the A-site cations in $LaMnO_3$ perovskites, which are not catalytically active, will preferentially occupy the native surface, resulting in unsatisfactory catalytic performance [22]. Researchers have worked extensively on this issue. It was proposed that the structural modification of perovskites by in situ heteroatom doping into the lattice framework could be a feasible and efficient strategy [23]. For example, the partial substitution of A-site La by some metal cations (e.g., Sr, K, Ce, Co) can regulate the valence state of the B-site active metal, promote rapid electron transfer, and improve the redox properties while maintaining structural stability [24–26]. Fe has also been shown to be a promising dopant for the A/B-site of $LaMnO_3$, where the doping at B-site could improve the concentration of reactive oxygen species and reducibility in the degradation of o-xylene, and the A-site doping promoted the reactivity and thermal stability in chemical looping reforming of methane [4,27]. However, to the best of our knowledge, few studies are devoted to the role of Fe for the A-site doped $LaMnO_3$ in VOCs oxidation.

Herein, in this work, a series of Fe doped $LaMnO_3$ at A-site photothermal catalysts ($La_{1-x}Fe_xMnO_3$, $0 \leq x \leq 0.2$) were synthesized via sol-gel method, and their physicochemical properties were characterized. Their PTCO performance of toluene was evaluated under full spectrum illumination, and it was further unraveled that the photothermal activity mainly derived from the light-driven heat. The results also showed that Fe doping and photoactivation synergistically promoted the oxidation of toluene. By combining multiple analytical techniques, the mechanistic details of the advanced activity driven by Fe doping and photoactivation were thoroughly studied. The mobility and activation of lattice oxygen species were found to play the primary role. Moreover, we proposed the possible pathways for toluene oxidation, and the co-effect of Fe doping and photoactivation on catalysts resistance and durability was also investigated. It is envisaged that the elucidation of Fe doping and photoactivation effects gives a more explicit direction for developing effective photothermal perovskite catalysts for environmental preservation.

2. Experimental section

2.1. Samples preparation

$La_{1-x}Fe_xMnO_3$ samples ($x = 0, 0.05, 0.10, 0.15, 0.20$) were synthesized via citrate sol-gel method. More details can be found in the Text S1 of Supplementary Information.

2.2. Samples characterization

The physicochemical properties of samples were investigated by diverse techniques, including X-ray diffraction (XRD), scanning electron microscopy (SEM), Brunauer-Emmett-Teller (BET), inductively coupled plasma optical emission spectrometry (ICP-OES), X-ray photoelectron spectroscopy (XPS), Fourier transform infrared spectroscopy (FTIR), UV–VIS-IR diffuse reflectance spectroscopy (DRS), electron paramagnetic resonance (EPR), temperature-programmed desorption of O_2 (O_2-TPD), temperature-programmed reduction of H_2 (H_2-TPR), temperature-programmed reduction of CO (CO-TPR), in situ diffuse reflectance infrared Fourier transform spectroscopy (in situ DRIFTS),

and $^{18}O_2$ isotope tracing experiment. The detailed characterization methods were described in the Text S2.

2.3. Calculation method

Density functional theory (DFT) calculations were conducted by Vienna Ab initio Simulation Package (VASP, version 6.2.1). The perovskite structure Fe doped $LaMnO_3$ models ($La_{0.9}Fe_{0.1}MnO_3$) were generated based on the (110) surface of standard perovskite structure ($Pm-3m$ (221)) $LaMnO_3$ system (Fe: La=1: 9), and selected the optimal one (constructure II) from three different constructions (Fig. S1), the optimized structure of $LaMnO_3$ and $La_{0.9}Fe_{0.1}MnO_3$ were also presented. More details on the calculations were provided in Text S3.

2.4. Catalytic performance evaluation

2.4.1. Photothermal catalytic activity

As shown in Fig. S2, the photothermal catalytic performance of $La_{1-x}Fe_xMnO_3$ ($0 \leq x \leq 0.2$) for toluene was evaluated in a cylindrical stainless-steel reactor with a quartz window under a 300 W Xe lamp (PLS-SXE300+, $\lambda= 320-2500$ nm). The light intensity was adjusted between 0.7 and 1.3×10^4 W/m^2 (corresponding 7–13 SUN intensity). The 0.1 g catalyst was later coated on the sand core with a diameter of 80 mm, and the surface temperature was measured by locating a thermocouple on the center of the catalyst layer. The simulated air flow (20% O_2/N_2) carrying 500 ppm toluene was passed through the catalyst layer at a total flow rate of 50 mL/min, giving a gas hourly space velocity (GHSV) of 30,000 mL/(g•h). In the case of water vapor introduction, 3–15 vol% H_2O was introduced by passing the feed stream through a water saturator at a certain temperature. For introducing SO_2, 100 ppm SO_2 from a 2000 ppm SO_2 cylinder (balanced with N_2) was introduced to the reaction system via a mass flow controller.

Prior to illumination, the sample was pretreated under simulated air flow at room temperature for 1 h, enabling adsorption-desorption equilibrium of toluene on the catalyst layer. The concentration of toluene was monitored by an online gas chromatograph (GC, GC-2014C, SHIMADZU) equipped with a flame ionization detector (FID), and CO_2 as the final product was detected by PGA-650 (Phymetrix, USA). The toluene conversion and CO_2 yield were calculated by Eqs. (1) and (2), respectively. The standard deviations were calculated from the repeated measurements of catalytic performance curves, and the standard deviations were all below 3%.

Additionally, the turnover frequencies (TOF, S^{-1}) values, Fe content and surface area normalized reaction rates (r_{Fe}^*, mol·g_{Fe}^{-1}·s^{-1}, $r_{S_{BET}}^*$, mol·m^{-2}·s^{-1}) were calculated in Text S4.

$$\text{Toluene conversion (\%)} = \frac{[\text{Toluene}]_{in} - [\text{Toluene}]_{out}}{[\text{Toluene}]_{in}} \times 100\% \quad (1)$$

$$\text{CO}_2 \text{ yield (\%)} = \frac{[\text{CO}_2]_{produced}}{[\text{CO}_2]_{theoretical}} \times 100\% \quad (2)$$

Where $[\text{Toluene}]_{in}$ and $[\text{Toluene}]_{out}$ represent the inlet and outlet concentration of toluene, respectively; $[\text{CO}_2]_{produced}$ and $[\text{CO}_2]_{theoretical}$ are the concentration of CO_2 produced in outlet gas and the theoretical value for complete conversion of toluene, respectively.

2.4.2. Thermocatalytic activity

The thermocatalytic oxidation (TCO) activity of the samples for toluene was evaluated on a tubular quartz reactor (i.d.= 6.00 mm, length= 600 mm) at different temperatures. The catalyst dosage, toluene concentration, gas component, and flow rate were consistent with the PTCO conditions. The experimental procedure was detailed in our previous publication [28].

3. Results and discussion

3.1. Catalytic performance

The PTCO performance of $La_{1-x}Fe_xMnO_3$ ($0 \leq x \leq 0.2$) samples with varied light intensity for gaseous toluene was evaluated under full spectrum (UV–VIS–IR) illumination. As illustrated in Fig. 1a and b, with the elevated light intensity from 0.7, 0.9, 1.1–1.3 $\times 10^4$ W/m^2, the toluene conversion and CO_2 yield of all samples increased markedly, and the CO_2 yield displayed a transient and abrupt rise after raising the illumination intensity, which probably due to the decomposition of accumulated intermediates. Obviously, Fe doping improved the catalytic activity and selectivity significantly. After the light illumination of 1.3×10^4 W/m^2 for 90 min, their performance followed the sequence: $La_{0.9}Fe_{0.1}MnO_3 > La_{0.95}Fe_{0.05}MnO_3 > La_{0.85}Fe_{0.15}MnO_3 > La_{0.8}Fe_{0.2}MnO_3 > LaMnO_3$, where $La_{0.9}Fe_{0.1}MnO_3$ performed the best with maximum toluene conversion of 86.7% and CO_2 yield of 84.6%. Notably, as a control, the commercial TiO_2 (P25) showed quite inert in the PTCO of toluene (Fig. S3). And for comparison with previously reported photothermal catalysts (Table S1), $La_{0.9}Fe_{0.1}MnO_3$ also exhibits remarkable performance. Interestingly, $La_{0.95}Fe_{0.05}MnO_3$ exhibited a greater improvement at lower light intensity of 0.7 and 0.9 $\times 10^4$ W/m^2, whereas the $La_{0.85}Fe_{0.15}MnO_3$ and $La_{0.8}Fe_{0.2}MnO_3$ improved poorly. This phenomenon indicates that the effect on the catalytic performance varies with the amount of Fe doping. Since La in $LaMnO_3$ was usually inert species and not involved in the catalytic reaction, while the B-site Mn was catalytically active, we calculated the TOF per unit amount of Mn ions to assess the effect of Fe doping at a conversion less than 20% [17]. The results in Table S2 showed that the $La_{0.9}Fe_{0.1}MnO_3$ exhibited the highest TOF values. Furthermore, by normalizing the toluene reaction rate with Fe weight, their catalytic performance was contrasted with excluding minor differences in Fe doping among samples. As Table S2, $La_{0.9}Fe_{0.1}MnO_3$ also exhibited the highest reaction rate, both normalized by Fe content (1.03×10^{-5} mol·g_{Fe}^{-1}·s^{-1}) and surface area (2.96×10^{-7} mol·m^{-2}·s^{-1}). Therefore, we suggest that the beneficial interaction between Fe and $LaMnO_3$ has no linear relationship with the content of Fe doping, and when the appropriate amount of Fe is 0.1, it gives a more desirable performance.

Additionally, the long-term PTCO performance of $La_{0.9}Fe_{0.1}MnO_3$ was tested under the light illumination of 1.3×10^4 W/m^2. As shown in Fig. 1c, the toluene conversion and CO_2 yield only exhibited a slight decrease in a 34 h toluene stream (500 ppm), illustrating outstanding durability. And the stability of $La_{0.9}Fe_{0.1}MnO_3$ was investigated by repeatedly changed the light intensity, the results of Fig. S4 showed the excellent stability of $La_{0.9}Fe_{0.1}MnO_3$. We also conducted the cyclic tests (2 h per cycle) to measure the cyclability of $La_{0.9}Fe_{0.1}MnO_3$. It could be seen from Fig. 1d, after 8 th cycle, the toluene conversion and CO_2 yield were still kept as high as 85.7% and 83.3%, respectively. These are important indicators to evaluate whether the catalyst has potential applicability in the real exhaust, the $La_{0.9}Fe_{0.1}MnO_3$ with excellent durability, stability and cyclability is expected to be a promising photothermal catalyst in practical application.

3.2. Origin of activity

According to the synergistic mode, photothermal catalysis can be classified into thermal-assisted photocatalysis, light-assisted thermal catalysis, light-driven thermal catalysis, and photothermal co-catalysis [12]. To deeply understand the PTCO mechanism over $La_{1-x}Fe_xMnO_3$ ($0 \leq x \leq 0.2$) samples, it is necessary to figure out the origin of activity. Thereby, the optical absorption capacity of all samples (Fig. 2a) was first investigated. The $LaMnO_3$ exhibited intense absorption between 200 nm and 2500 nm, processing great ability in light utilization, which was consistent with the previous reports [17,19]. After the doping of Fe, the samples maintained a broad and intense absorption. However, it was weakened with the increase of Fe content, especially in the IR region. Generally, the samples with strong absorption in the VIS–IR region enable it a highly active photothermal responsive that absorbs light and releases the absorbed photons as heat efficiently. To further measure the photothermal conversion ability of samples, their equilibrium temperature under light illumination was recorded as Fig. 2b. The sequencing of the equilibrium temperature on these samples corresponded well to the DRS results. Such energy supply from the effective photo-thermal conversion could maintain the surface temperature of samples at about 180 °C, thus potentially driving the occurrence of some endothermic reactions, such as the oxidation of toluene.
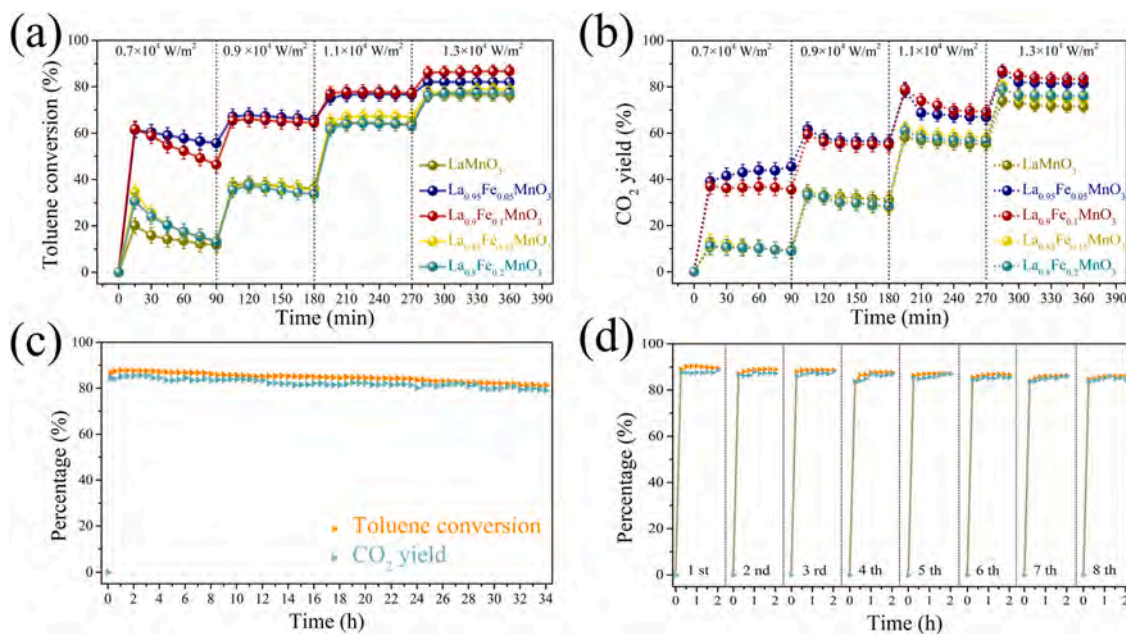

Fig. 1. (a) Toluene conversion and (b) CO_2 yield over $La_{1-x}Fe_xMnO_3$ ($0 \leq x \leq 0.2$) samples with varied light intensity under full spectrum illumination. The durability (c) and cyclability tests (d) of PTCO performance on $La_{0.9}Fe_{0.1}MnO_3$. (Reaction condition: 500 ppm toluene, 20 vol% O_2/N_2, light intensity=1.3×10^4 W/m^2).
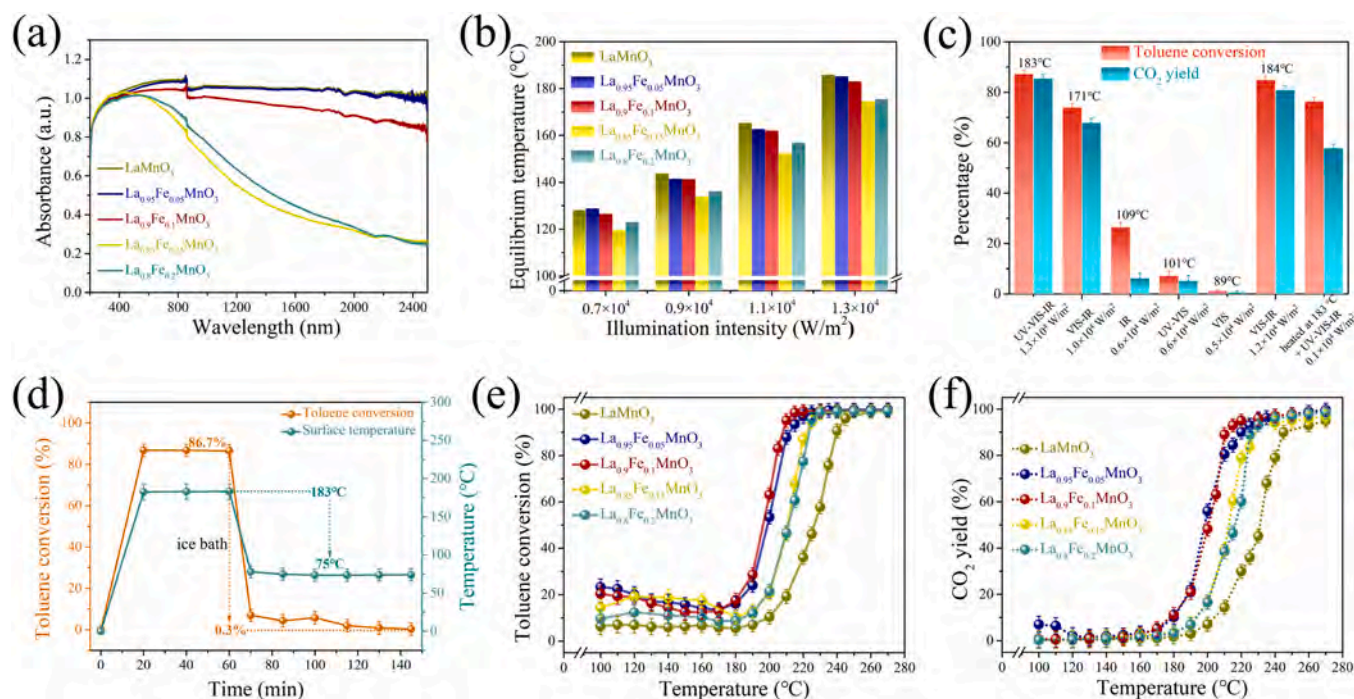
Fig. 2. (a) UV–VIS–IR DRS and (b) equilibrium temperature under light illumination of La$_{1-x}$Fe$_x$MnO$_3$ ($0 \leq x \leq 0.2$) samples. (c) The toluene conversion and CO$_2$ yield over La$_{0.9}$Fe$_{0.1}$MnO$_3$ under different wavelengths of light illumination (UV–VIS–IR, VIS–IR, IR, UV–VIS and VIS). (d) The variation of PTCO activity and surface temperature on La$_{0.9}$Fe$_{0.1}$MnO$_3$ under an ice water bath. (e) The toluene conversion and (f) CO$_2$ yield of La$_{1-x}$Fe$_x$MnO$_3$ ($0 \leq x \leq 0.2$) samples under traditional TCO reaction.

As we known, the short-wavelength UV light are the primary energy source for traditional PCO, while long-wavelength VIS and IR spectra can hardly excite the photogenerated carriers, their contribution to some redox reactions is mainly attributed to their thermal effects [16, 29]. To investigate whether the photothermal catalysis on La$_{0.9}$Fe$_{0.1}$MnO$_3$ has both PCO and TCO reactions going on simultaneously, we placed the cut-off filters (420 nm and/or 800 nm) between the Xe lamp and quartz window to subdivide the UV–VIS–IR light into VIS–IR, IR, UV–VIS and VIS regions, as shown in Fig. 2c. Obviously, the activity under VIS–IR light illumination was much higher than that of IR, UV–VIS and VIS light, but lower than UV–VIS–IR light. When enhancing the VIS–IR light intensity until the induced temperature was close to that of UV–VIS–IR light, the activity of the two differed little. It implied that the VIS–IR light played a more critical role, which provided the required heat energy to trigger the oxidation of toluene over La$_{0.9}$Fe$_{0.1}$MnO$_3$. When controlling the light intensity of VIS–IR, IR, UV–VIS and VIS consistent with the UV–VIS–IR light (Fig. S5), the activity showed a similar trend as that of Fig. 2c. Notably, under the relatively low UV–VIS–IR light illumination of 0.1×10^4 W/m^2 and heated at 183 °C simultaneously, the activity showed a slight decrease, which suggested that light also had an activation effect and related with intensity. Interestingly, we placed it in an ice water bath, and further estimated the activity under light illumination of 1.3×10^4 W/m^2 at low temperatures (Fig. 2d). It was found that the surface temperature was rapidly decreased from 183 °C to 77 °C due to the heat dissipation, which caused the toluene conversion plummeted and closed to 0%. Besides, there was feeble and no significant signal change of the photogenerated free radicals (·OH, ·O$_2^-$) at dark and light illumination (Fig. S6). The results indicated that the contribution of traditional PCO was relatively insignificant or even negligible, and the activation of light acted on the basis of thermal effects.

In general, it can be argued that the excellent PTCO activity of La$_{0.9}$Fe$_{0.1}$MnO$_3$ originates from light-driven thermal catalysis with the activation of light. Owing to its excellent photothermal conversion ability, it can rapidly convert the absorbed light (mainly the VIS–IR

region) into heat, which increases the temperature of the local active sites, and suffices to induce the oxidation of toluene. Traditional TCO experiments also confirmed it. As presented in Fig. 2e and f, their sequence of TCO activity was consistent with that of PTCO, with the best performance of La$_{0.9}$Fe$_{0.1}$MnO$_3$ (T_{90}= 208 °C). And toluene began to be oxidized at around 180 °C, which meant that the equilibrium temperature (183 °C) of La$_{0.9}$Fe$_{0.1}$MnO$_3$ under UV–VIS–IR illumination could reach the light-off temperature for toluene oxidation. Thus, the light-driven thermal catalysis of toluene could occur. In addition, the equilibrium temperature of La$_{0.9}$Fe$_{0.1}$MnO$_3$ under IR illumination (109 °C) was much lower than the T$_{light-off}$ but still showed a certain activity, which further illustrated the existence of photoactivation. It was consistent with the report of Yu et al. [18]. In conclusion, the Fe doping and photoactivation effect both significantly impact the catalytic performance of LaMnO$_3$. But how Fe doping and photoactivation affect the catalytic performance for toluene, as well as the specific reaction pathways and mechanisms, are subject to be illustrated by further detailed characterizations and DFT calculations.

3.3. The effect of Fe doping

3.3.1. Crystal phase structure

Fig. 3 shows the XRD patterns of La$_{1-x}$Fe$_x$MnO$_3$ ($0 \leq x \leq 0.2$) samples. The diffraction peaks located at about 22.9°, 32.6°, 40.2°, 46.8°, 52.7°, 58.2°, 68.3°, 73.2°, and 77.8° can be indexed to the (100), (110), (111), (200), (210), (211), (220), (300), and (310) crystal planes of LaMnO$_3$ (JCPDS PDF #75–440), which suggests the successful synthesis of a well single-phase LaMnO$_3$ perovskite. After Fe doping, there was no significant shift in the characteristic peaks, but became broader and weaker sequentially with increasing Fe content. It was indicated that Fe doping could suppress the crystallization of LaMnO$_3$ and lead to more non-crystalline phases [30], thus reducing the crystallite size (Table 1). Moreover, the cell volumes of La$_{1-x}$Fe$_x$MnO$_3$ (347.61–348.57 Å^3) were shown to be reduced than that of LaMnO$_3$ (349.26 Å^3), which could be ascribed to the partial substitution of the smaller ionic radius of Fe^{3+}
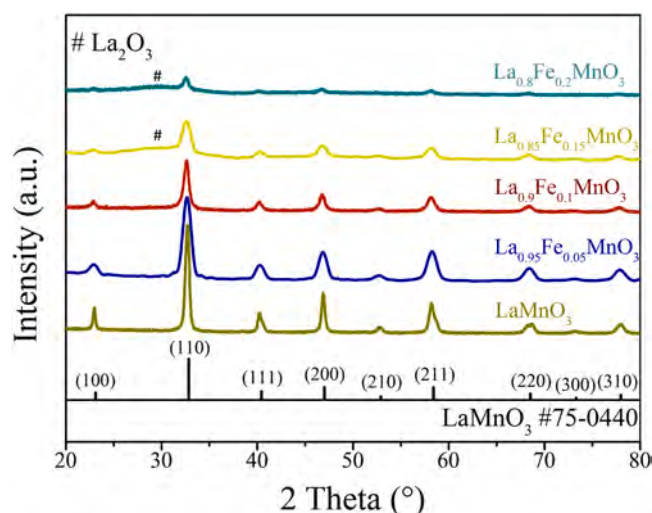
Fig. 3. XRD patterns of La$_{1-x}$Fe$_x$MnO$_3$ ($0 \leq x \leq 0.2$) samples.

(0.62 Å) for La^{3+} (1.17 Å), and lead to the cell lattice shrinkage and distortion [25,27]. It might further induce the generation of lattice defects [25]. Notably, no characteristic peaks of Fe species were observed, suggesting Fe cations might incorporate into the lattice of LaMnO$_3$ and were highly distributed [4]. And a newly weak diffraction peak located at 29.9° was detected on La$_{0.85}$Fe$_{0.15}$MnO$_3$ and La$_{0.8}$Fe$_{0.2}$MnO$_3$, which was assigned to the (101) lattice planes of hexagonal La$_2$O$_3$ (JCPDS PDF #74–2430). The presence of La$_2$O$_3$ impurity could attribute to the surface enrichment of La species during calcination, which discouraged the formation of the perovskite phase and led to the decrease in catalytic activity [31].

3.3.2. Morphological and textural properties

The morphologies of the samples were characterized by SEM, as depicted in Fig. S7. All samples have a bulk structure with spongy-like surface consisting of agglomerates and numerous pores, which favors the exposure of active sites. Such morphology is a consequence of the thermal decomposition of citric acid [32].

Fig. 4 presents the N$_2$ adsorption-desorption isotherms and pore size distribution curves. At the relative high-pressure ratio (P/P$_0$= 0.4–1.0), all samples possess the typical IV isotherms with an H3 type hysteresis loop, which indicates the presence of mesoporous structures. And their particle sizes are basically clustered between 2 and 20 nm, which affirms this inference. Moreover, as shown in Table 1, with increased Fe content, the pore size of samples exhibited a decreasing trend (from 11.3 to 8.0 nm), suggesting the structure transformed from the stacked state to a loose state. While their specific surface area and pore volume were increased with Fe content, which was consistent with the XRD results and suggested the inhibition of crystallization [29]. Thereinto, La$_{0.8}$Fe$_{0.2}$MnO$_3$ showed the highest specific surface area (43.5 m^2/g)

and pore volume (0.106 cm^3/g), which was believed to benefit the adsorption/oxidation of toluene. However, the actual catalytic performance lacked a linear correlation with these textural properties, hence it might not be the dominant factor.

3.3.3. Surface chemical states

The XPS technique was utilized to evaluate the surface elementary composition and chemical states (La 3d, Mn 2p, and Fe 2p) of La$_{1-x}$Fe$_x$MnO$_3$ ($0 \leq x \leq 0.2$) samples (Fig. 5a), and the corresponding quantitative results were summarized in Table 2. It was worth mentioning that the (La+Fe)/Mn molar ratio of the La$_{1-x}$Fe$_x$MnO$_3$ ($0 \leq x \leq 0.2$) samples was approached 1.0, and the doping amount of Fe was also agreed well with the theoretical value (Table 1), which indicated that Fe successfully substituted La in the A-site instead of Mn in the B-site.

As shown in Fig. 5b, the spin-orbit splitting of La 3d is around 16.8 eV for all samples, suggesting the trivalent state of La [33]. Obviously, the peaks of La 3d$_{5/2}$ and La 3d$_{3/2}$ slightly shifted toward lower binding energy as the Fe content increased, which could be attributed to the elevated electron density around La cations [34]. And there was no significant change in the main peaks, implying La species possessed a relatively stable chemical environment. The Mn 2p spectra (Fig. 5c) is divided into two components, where the peaks at 641.8–641.9 eV correspond to Mn^{3+} species, and the peaks at 643.1–643.4 eV can be assigned to Mn^{4+} species [17]. As presented in Table 2, the Mn^{4+}/Mn^{3+} molar ratio of La$_{1-x}$Fe$_x$MnO$_3$ ($0 \leq x \leq 0.2$) decreased to 0.65–0.69 by comparison with LaMnO$_3$ (1.17), implying that Fe doping had led to more low-valence Mn^{3+}. While the lower manganese state (Mn^{3+})
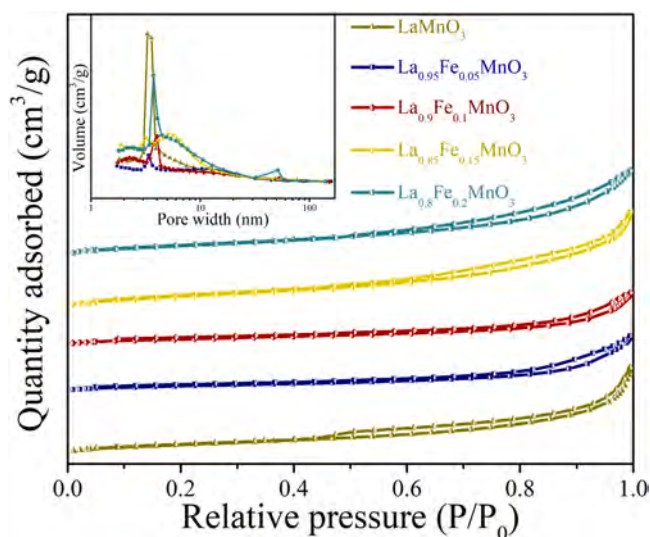

Fig. 4. N$_2$ adsorption-desorption isotherms and pore size distribution curves (inset) of La$_{1-x}$Fe$_x$MnO$_3$ ($0 \leq x \leq 0.2$) samples.

Table 1
The textural parameters of as-prepared samples (theoretical values in brackets).

Sample	Fe doping[a] (wt %)	Surface area[b] (m^2/g)	Pore volume[c] (cm^3/g)	Mean diameter[c] (nm)	Crystal size[d] (nm)	Lattice constant[d] (Å)			Cell volume[d] (Å^3)
						a	b	c	
LaMnO$_3$	/	31.9	0.101	9.3	14.9	5.498	5.498	13.342	349.26
La$_{0.95}$Fe$_{0.05}$MnO$_3$	1.14 (1.18)	19.2	0.063	11.3	12.2	5.494	5.494	13.296	348.57
La$_{0.9}$Fe$_{0.1}$MnO$_3$	2.35(2.39)	28.6	0.064	9.7	11.6	5.489	5.489	13.291	348.38
La$_{0.85}$Fe$_{0.15}$MnO$_3$	3.41 (3.65)	36.1	0.104	9.0	11.6	5.485	5.485	13.306	347.96
La$_{0.8}$Fe$_{0.2}$MnO$_3$	4.81 (4.96)	43.5	0.106	8.0	10.5	5.482	5.482	13.307	347.61

[a] The doping content of Fe was calculated by ICP-OES results.
[b] The specific surface area was calculated based on N$_2$ adsorption–desorption by the BET method.
[c] The pore volume and mean pore diameter was calculated by the BJH method.
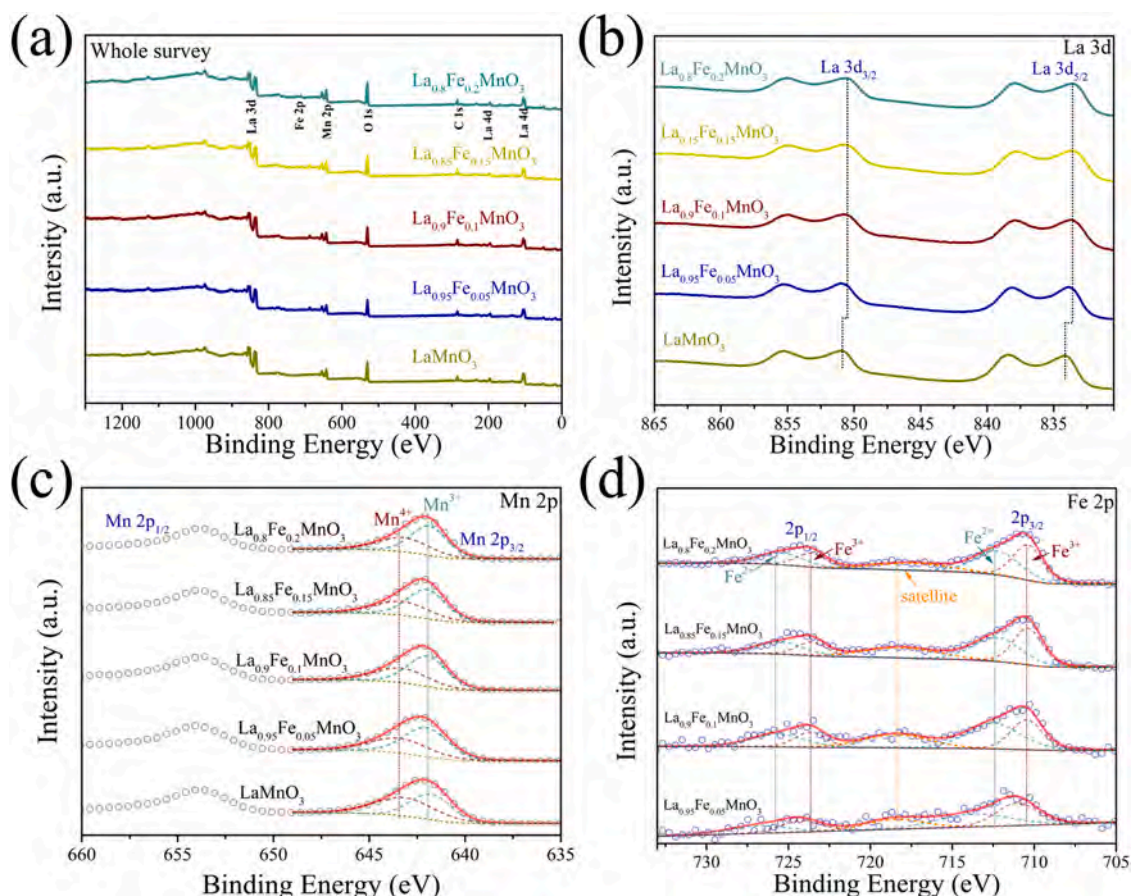[d] The lattice parameter was obtained by XRD patterns.

Fig. 5. (a) The full XPS spectra and high resolution XPS scans of (b) La 3d, (c) Mn 2p and (d) Fe 2p for $La_{1-x}Fe_xMnO_3$ ($0 \leq x \leq 0.2$) samples.

Table 2
The surface chemical states and quantitative results of as-prepared samples.

Sample	Molar ratio of (La+Fe)/Mn[a]	Mn 2p[a] Mn⁴⁺/Mn³⁺	Fe 2p[a] Fe³⁺/Fe²⁺	O 1 s[a] O_{latt}/O_{ads}	O₂ consumption (mmol/g)[b] 100–300 °C	300–600 °C	600–900 °C	Total	H₂ consumption (mmol/g)[c] 100–500 °C	500–800 °C	Total
$LaMnO_3$	1.03	1.17	/	1.13	0.056	0.342	0.551	0.949	1.822	1.670	3.492
$La_{0.95}Fe_{0.05}MnO_3$	1.09	0.67	0.99	1.46	0.315	0.307	1.099	1.721	1.865	1.769	3.634
$La_{0.9}Fe_{0.1}MnO_3$	0.97	0.65	1.45	1.48	0.073	0.657	1.418	2.148	3.760	0.796	4.756
$La_{0.85}Fe_{0.15}MnO_3$	0.98	0.68	1.16	1.39	0.081	0.477	1.527	2.085	3.993	0.821	4.814
$La_{0.8}Fe_{0.2}MnO_3$	0.93	0.69	1.08	0.98	0.076	0.504	1.510	2.09	4.077	0.808	4.885

[a] Calculated by the XPS results.
[b] O₂ consumption from O₂-TPD profiles.
[c] H₂ consumption from H₂-TPR profiles.

present in the crystal can promote the mobility of lattice oxygen and affect the surface reactive oxygen species [35]. These properties were reported to facilitate the redox reaction of toluene [29].

For Fe species (Fig. 5d), two main asymmetric peaks are located at around 710.8 eV and 723.9 eV, which are assigned to the Fe $2p_{3/2}$ and Fe $2p_{1/2}$, respectively (spin-orbital splitting of 13.2 eV) [25]. And the other peak at about 718.3 eV corresponds to the shake-up satellite, indicating the presence of surface Fe^{3+} [36]. The Fe $2p_{3/2}$ orbit can split into two peaks, which are attributed to Fe^{2+} (710.4–711.0 eV) and Fe^{3+} (712.2–713.7 eV), accordingly [37]. The valence state transformation of the Fe cations from +2 to +3 indicated a significant change in the electronic structure, which also verified the successful doping of Fe to the $LaMnO_3$ lattice [38]. Notably, the high-valence Fe^{3+} can act as the active site for toluene oxidation, and its concentration in $La_{0.9}Fe_{0.1}MnO_3$ is the highest of all samples (Fe^{3+}/Fe^{2+}=1.45). Combined with the decrease of Mn^{4+}/Mn^{3+} after Fe doping, we speculated there was an

intense interaction between Fe and Mn species, which greatly accelerates electron transfer and meets the needs of multi-electron reaction (e. g., toluene oxidation). In addition, after PTCO or TCO reactions (Fig. S8), the peak position of surface Mn^{4+} and Fe^{3+} on $La_{0.9}Fe_{0.1}MnO_3$ moved to higher binding energy, and the ratio of Mn^{4+}/Mn^{3+} and Fe^{3+}/Fe^{2+} were differentially reduced (Table S3). The results suggest that the surface Mn^{4+} and Fe^{3+} as the active components are involved in the redox reaction of toluene.

3.3.4. Reactive oxygen species

Generally, reactive oxygen species are tightly involved in the adsorption/activation of VOCs molecules, especially lattice oxygen plays an essential role in the Mars-van-Krevelen mechanism for the oxidation of aromatic VOCs [17]. Accordingly, we applied the XPS, TPD, TPR techniques to reveal the types and properties of reactive oxygen species in the as-prepared samples. And DFT calculations were
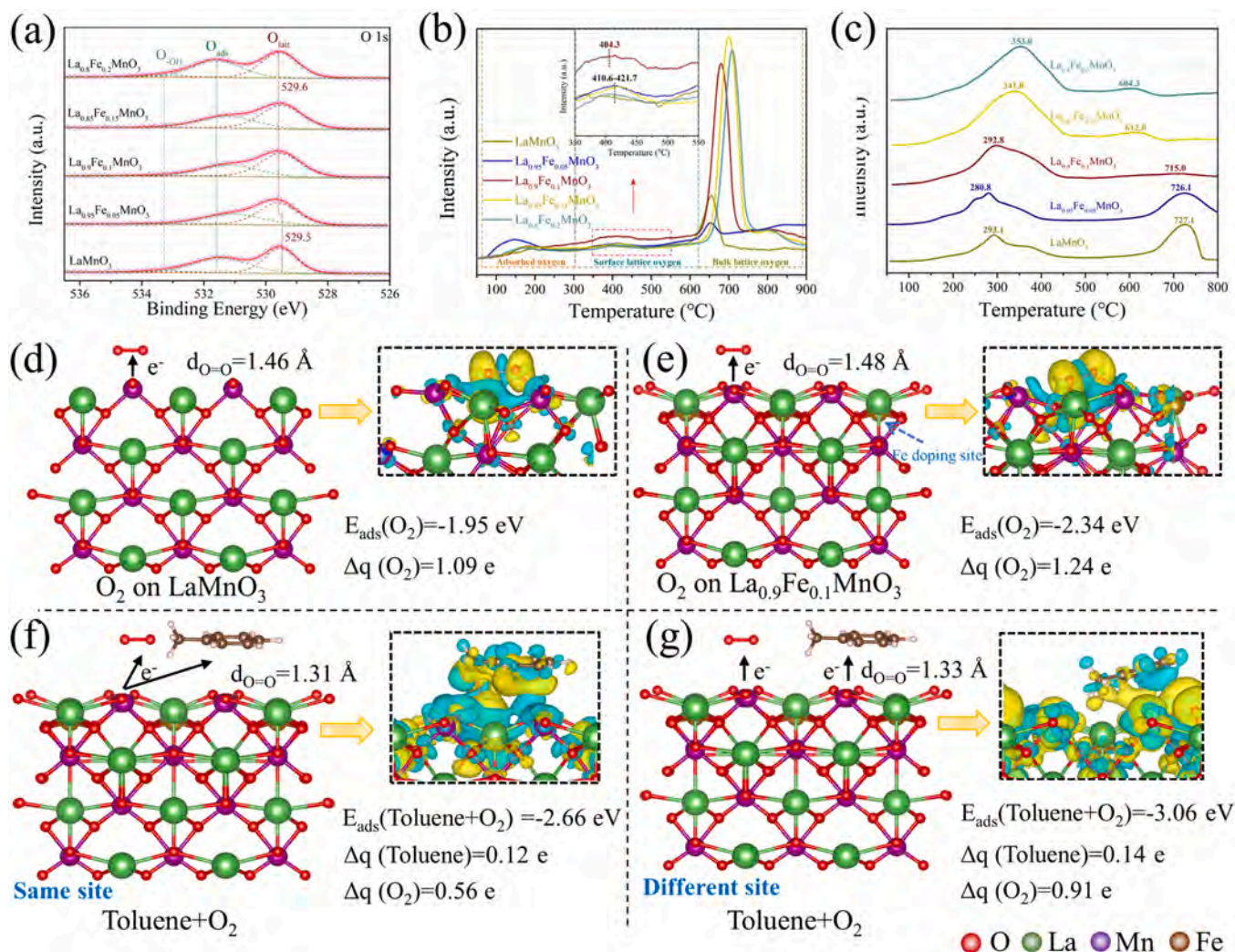
Fig. 6. (a) O 1 s XPS spectra, (b) O_2-TPD profiles (the inset is an enlarged part from 350 °C to 550 °C), and (c) H_2-TPR profiles of $La_{1-x}Fe_xMnO_3$ ($0 \leq x \leq 0.2$) samples. The O_2 adsorption simulation of (d) $LaMnO_3$ and (e) $La_{0.9}Fe_{0.1}MnO_3$. The O_2 and toluene co-adsorption at same (f) and different sites (g) simulation of $La_{0.9}Fe_{0.1}MnO_3$. The isosurfaces are set to 0.002 eV•Å^{-3}.

conducted to investigate the effect of O_2 for adsorption/activation of toluene.

As shown in Fig. 6a, the O 1 s spectra are used to identify the surface oxygen species. The peaks at around 529.5–529.6 eV, 531.1–531.6 eV, and 533.4 eV can be assigned to surface lattice oxygen (O_{latt}), surface adsorbed oxygen (O_{ads}), and hydroxyl/adsorbed molecular water (O_{-OH}), respectively [29]. The associated quantitative results are summarized in Table 2. As a symbol of the intrinsic relationship between reducibility and oxygen species, the atomic ratio of O_{latt}/O_{ads} was increased substantially after Fe doping, which might be related to the valence variation of the metal species [30]. Thereinto, the $La_{0.9}Fe_{0.1}MnO_3$ showed the highest value of 1.48 compared to $LaMnO_3$ (1.13), demonstrating that the Fe had a significant impact on the reactive oxygen species. Moreover, the peaks of O_{latt} inclined to slightly shift toward higher binding energy, which could ascribe to the decrease in electron density around O_{latt} [39]. The O_{latt} atoms may bond less tightly in the structure, and lead to higher mobility [40].

O_2-TPD was applied to further investigate the mobility of oxygen species. As presented in Fig. 6b, which are divided into three regions. In the low-temperature region of 50–300 °C, the oxygen desorption peaks belong to the chemisorbed oxygen species (O_2^- or O_2^{2-}) and physisorbed molecular oxygen [41]. For 300–600 °C, the peaks can be assigned to

the desorption of surface O_{latt} species (O^{2-}) generated by lattice defects [31]. At the high-temperature region (600–900 °C), the peaks are associated with the bulk O_{latt} species, which are usually accompanied by a decreased valence of the B-site metal cations in perovskite oxides [42]. Since the reaction usually proceeds at a relatively low temperature, the oxygen desorption behavior at low/middle temperatures deserves more attention. For $La_{0.95}Fe_{0.05}MnO_3$, the desorption area at the low temperature of 100–300 °C was enlarged significantly, implying a higher O_{ads} content. It is believed that the O_{ads} with strongly electrophilic can attack organic molecules readily [43]. Thereby, the $La_{0.95}Fe_{0.05}MnO_3$ could perform better at low light intensity (low temperatures). As for surface O_{latt} species, their desorption temperature is well correlated with mobility [17]. At the middle-temperature region (300–600 °C), $La_{0.9}Fe_{0.1}MnO_3$ exhibited a larger amount and lower desorption temperature than other samples, which indicated that the moderate doping of Fe could enhance the mobility of surface O_{latt} and accelerate oxygen species migration from subsurface to surface [17,29]. It was in agreement with the results of XPS. The enhanced mobility and amount of surface O_{latt} may be a major factor contributing to the promising PTCO performance on $La_{0.9}Fe_{0.1}MnO_3$. Moreover, as listed in Table 2, the total O_2 desorption of $LaMnO_3$ (0.949 mmol/g) was much less than that of Fe doped samples. The $La_{0.9}Fe_{0.1}MnO_3$ had the most O_2 consumption of

2.148 mmol/g, suggesting a larger amount of reactive oxygen species. It is probably explained by the fact that the doping of Fe can induce lattice defects that promote the mobility and/or activation of oxygen species [25].

TPR experiment is performed to study the reactivity of oxygen species. The H_2-TPR profiles are given in Fig. 6c. It is worth mentioning that La^{3+} is hardly reduced below 1000 °C, thus the discussion is based on the reduction of Mn and Fe cations. There are two clear H_2 consumption peaks in $LaMnO_3$, where the peak at low temperatures (100–500 °C) corresponds to the consumption of a small amount surface adsorbed oxygen, accompanied by the reduction of Mn^{4+} to Mn^{3+} and a single electron reduction of Mn^{3+} (located in a highly coordination-unsaturated microenvironment) to Mn^{2+}, while the second reduction peak (500–800 °C) is attributed to the reduction of the Mn^{3+} left in the $LaMnO_3$ lattice to Mn^{2+} [44]. After Fe doping, new reduction processes were occurring, which could be correlated with the surface Fe^{3+} to Fe^{2+} between 100 and 500 °C, and bulk Fe^{3+} to Fe^{2+}, Fe^{2+} to Fe^0 at temperatures exceeding 500 °C [4]. Obviously, the first reduction peak tended to shift toward higher temperatures with increased Fe content. Compared with $LaMnO_3$, $La_{0.95}Fe_{0.05}MnO_3$ and $La_{0.9}Fe_{0.1}MnO_3$ both exhibited a lower reduction temperature. It could be considered that the moderate doping of Fe improved the mobility of O_{latt} species [45], consistent with the results of XPS and O_2-TPD. Moreover, the H_2 consumption at low temperatures is informative for exploring the reducibility. As given in Table 2, the H_2 consumption of $La_{0.9}Fe_{0.1}MnO_3$ was significantly increased to 3.760 mmol/g between 100 and 500 °C, compared to that of $La_{0.95}Fe_{0.05}MnO_3$ with 1.865 mmol/g. It is commonly believed to be related to highly mobilized oxygen species, which explained the rapid generation of surface sites for H_2 adsorption [46]. And some reactive oxygen species (e.g., surface O_{latt}) are closely related to catalytic activity, which is mainly reflected by low-temperature reducibility. Therefore, $La_{0.9}Fe_{0.1}MnO_3$ with better mobility and quantity of surface O_{latt} may have stronger low-temperature reducibility despite its slightly higher reduction temperature than $La_{0.95}Fe_{0.05}MnO_3$.

In a typical VOCs oxidation process, the reoxidation of reduced metal species is well associated with the replenishment of surface O_{latt} from free O_2 [47]. To pursue long-term reaction durability, the availability of timely replenishment of consumed reactive oxygen species also needs to be evaluated. While O_2 molecules as the main source of oxygen species, are essential for VOCs oxidation. Thus, a comparison of O_2 simulated adsorption processes of $LaMnO_3$ and $La_{0.9}Fe_{0.1}MnO_3$ was performed by DFT calculations. As displayed in Fig. 6d and e, the absolute value of adsorption energy (E_{ads}) on $La_{0.9}Fe_{0.1}MnO_3$ (−2.34 eV) was much higher than $LaMnO_3$ (−1.95 eV), and the O−O bond length of O_2 on $La_{0.9}Fe_{0.1}MnO_3$ was extended to 1.48 Å, slightly longer than that on $LaMnO_3$ (1.46 Å). The results illustrate that O_2 molecules are more likely activated on $La_{0.9}Fe_{0.1}MnO_3$. Moreover, the electronic interaction between the O_2 and $La_{0.9}Fe_{0.1}MnO_3$ was stronger than $LaMnO_3$ from the differential charge density. And Bader charge calculation also confirmed this, the transferred charge (Δq) of O_2 on $La_{0.9}Fe_{0.1}MnO_3$ was 1.24 e, whereas that of $LaMnO_3$ was 1.09 e, implying that the O_2 obtained more electrons from $La_{0.9}Fe_{0.1}MnO_3$. Therefore, the charge transfer is easier between the O_2 and $La_{0.9}Fe_{0.1}MnO_3$. Combined with the stronger O_2 adsorption and activation, it is reasonable to speculate that the moderate doping of Fe will facilitate the formation and regeneration of reactive oxygen species, thus replenishing the consumed O_{latt} species and perpetuating reactions [47]. Furthermore, we investigated the co-absorption of O_2 and toluene on $La_{0.9}Fe_{0.1}MnO_3$ (Fig. 6f and g). As compared to separate absorption of O_2 (Fig. 6e) and toluene (Fig. S9), whether co-adsorbed of O_2 with toluene at the same sites or different sites, it was obvious that the presence of O_2 promoted the adsorption/activation of toluene. Notably, when co-adsorbed at different sites, the E_{ads} was much higher and electronic interaction (Δq, differential charge density) was more intense than that of at same sites, which might attribute to the competition absorption between O_2 and toluene. In fact,

when O_2 and toluene were adsorbed simultaneously, the electron transfer between O_2 and sample was reduced (especially co-adsorbed at same sites, the Δq decreased significantly from 1.24 e to 0.56 e), and this portion might contribute to the electronic interaction between toluene and sample (Δq (Toluene) was increased from 0.09 e to 0.12 e and 0.14 e), which could further promote the adsorption/activation of toluene.

3.4. The effect of photoactivation

In fact, in addition to the Fe doping, the photoactivation effect induced by light was also reported to affect the reactive oxygen species [18,29]. To further investigate the photoactivation effect, some characterizations and DFT calculations were performed.

As shown in Fig. 7a, the O peaks shifted toward higher binding energy after PTCO reaction, suggesting the O_{latt} was effectively activated [39]. Moreover, the O_{latt} was more significantly consumed after PTCO reaction, and the relative amount of O_{ads} was also found more than that of TCO (Table S3). In general, the generation of surface O_{ads} is usually associated with the adsorption of gaseous O_2, and it contributed to the replenishment of consumed O_{latt} species [47]. Yu et al. [29] reported that the photoactivation effect could activate more gaseous O_2 molecules, thus replenishing the surface O_{latt}. Therefore, it is reasonable to assume that light has a positive impact on activating oxygen species.

CO-TPR under illumination or at dark was also used to study the photoactivation effect. As displayed in Fig. 7b, a broad TPR peak appeared around 250 °C, which could be ascribed to the oxidation of CO by surface O_{latt} [48]. Obviously, the peak shifted to lower temperature under illumination, suggesting that the activity of O_{latt} was enhanced due to photoactivation. In addition, the CO consumption of $La_{0.9}Fe_{0.1}MnO_3$ was significantly increased from 247.0 µmol/g at dark to 311.7 µmol/g under illumination, which indicated that the light could activate more O_{latt} species to be involved in oxidation reactions.

DFT calculations were also performed to study the effect of light illumination on the O_{latt} activity over $La_{0.9}Fe_{0.1}MnO_3$ (Fig. 7c). Generally, the visible light absorption of metal oxides derived from the *d-d* transition, which induces the materials in the ground state to the excited state [49]. Accordingly, we applied the constrained occupancy DFT approach, and changed the *d* electron number in down and up spin components to calculate the energy of removing one O atom from materials in the excited state [50]. It could be observed that the ΔE of removing one O atom from $La_{0.9}Fe_{0.1}MnO_3$ was 0.665 eV, respectively, which was much lower than that of the ground state (2.092 eV). And that $LaMnO_3$ showed the same phenomenon (Fig. S10). It suggests that the activity of O_{latt} is enhanced by visible light, in agreement with the result of CO-TPR.

Furthermore, to investigate the catalytic behavior of the O_{latt} activated by light, in situ DRIFT was firstly carried out in Toluene/N_2 atmosphere. As observed from Fig. 8a, some typical characteristic absorbance bands of toluene appeared, and their intensity slightly increased with time. The peaks at around 1619, 1551, and 1464 cm^{-1} are ascribed to the C=C stretching vibration of the aromatic ring [51]. The bands at 2938 and 2874 cm^{-1} are from the C−H symmetric and asymmetric vibration of methylene (−CH_2) [52]. While under light illumination, these typical peaks were weakened or disappeared immediately. And some new peaks appear at 1594 and 1416 cm^{-1} are ascribed to the C=O stretching vibration of aldehydic species and −COO− stretch modes of benzoate species, respectively [29], demonstrating the formation of typical intermediates in toluene oxidation. In addition, the new peak at 1315 cm^{-1} is regarded as the maleic acid and maleic anhydride, and the band located at 1735 cm^{-1} belonging to chain fatty acid is also detected, which are important intermediates in the ring-opening process of toluene [11]. The results suggest that the oxidation of toluene can be conducted by using surface O_{latt} species activated by light in absence of O_2. However, since the O_{latt} is not available for timely replenishment, it is difficult to achieve the deep oxidation of toluene. To further discuss the pathway of toluene
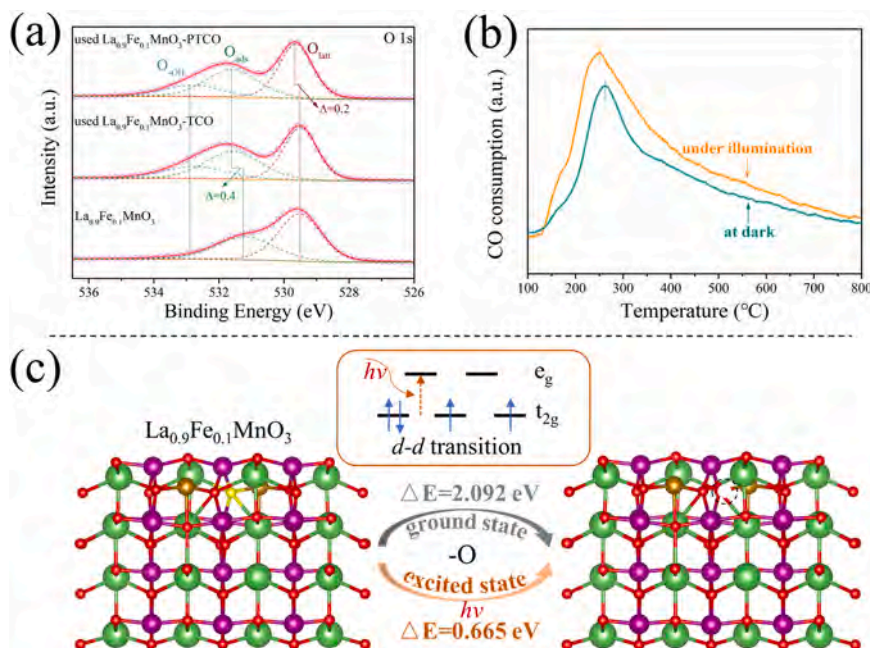
Fig. 7. (a) O 1 s XPS spectra of fresh and used $La_{0.9}Fe_{0.1}MnO_3$ after PTCO or TCO reactions. (b) CO-TPR profile of $La_{0.9}Fe_{0.1}MnO_3$ under Xe lamp illumination and at dark. (c) Calculated energy of removing one O atom (yellow sphere) from the $La_{0.9}Fe_{0.1}MnO_3$ in the ground or excited states. (PTCO reaction condition: 500 ppm toluene, 20 vol% O_2/N_2, light intensity$=1.3 \times 10^4$ W/m^2; TCO reaction condition: 500 ppm toluene, 20 vol% O_2/N_2, 183 °C).

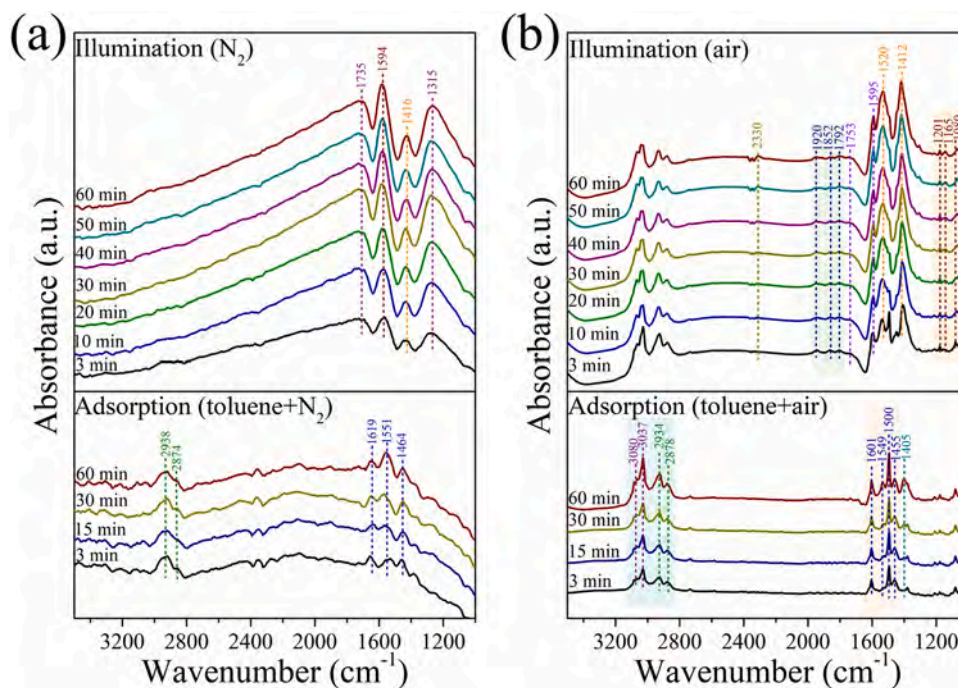**Fig. 8.** *In situ* DRIFT spectra of toluene adsorption and oxidation on $La_{0.9}Fe_{0.1}MnO_3$ in (a) N_2 and (b) air.

degradation, it is essential to investigate the adsorption and oxidation behavior in the air atmosphere. As shown in Fig. 8b, after introducing toluene, the typical aromatic ring vibrations at 1601, 1549, 1500 and 1455 cm^{-1} were observed immediately, and their intensity increased with time [43,51]. In the C−H stretching region (3100–2850 cm^{-1}), the bands at 3080 and 3037 cm^{-1} belong to the aromatic ring, and the bands at 2934 and 2878 cm^{-1} are attributed to methylene (−CH$_2$). Moreover, the peak corresponding to the bending vibration of CH$_2$ is detected at 1405 cm^{-1} [53]. These results suggest that the toluene can be more strongly adsorbed on the catalyst through its methyl group in air. While

under light illumination, the weak bands at 1920, 1852, and 1792 cm^{-1} associated with the maleic anhydride are observed, and also detect the characteristic band of final product CO$_2$ at 2330 cm^{-1}, which illustrates the occurrence of oxidation reactions [54]. In contrast, the spectra remain almost unchanged after heating to 183 °C (agreeing with the light-induced equilibrium temperature) in the dark (Fig. S11). The results revealed that light could effectively activate O$_{latt}$ species to be involved in the oxidation of toluene.

Moreover, similar to the experiments in the N$_2$ atmosphere, new characteristic bands of some important intermediates appeared. The

weak bands at 1201, 1165, and 1080 cm^{-1} are regarded as the C−O stretching vibration of benzyl alcohol [11,51]. The strong bands at 1520 and 1412 cm^{-1} can be assigned to the −COO− stretching vibrations of benzoate species, demonstrating the formation of benzoic acid directly [55]. The bands at 1753 and 1595 cm^{-1} assigned to aldehydic species indicate the formation of benzaldehyde [56]. Notably, these bands (especially the bands belonging to the benzoate species) continued to increase and became the prominent peaks, which suggested that benzyl alcohol, benzoic acid, and benzaldehyde are the key intermediates in the deep oxidation of toluene to CO_2 and H_2O, and toluene oxidation follows the benzoate reaction route [57]. In the presence of O_2, consumed O_{latt} gets timely replenishment, thus the oxidation pathway of toluene is slightly changed, allowing toluene to be degraded more deeply.

Moreover, to better understand the role of O_{latt} on toluene oxidation, the $^{18}O_2$ isotope experiment was further carried out under light illumination, and the reaction products ($C^{16}O_2$, $C^{16}O^{18}O$, $C^{18}O_2$) were detected (Fig. 9a). Obviously, the $C^{18}O_2$ was generated abundantly, meanwhile the $C^{16}O_2$ was also produced due to the involvement of O_{latt}. However, as the reaction proceeded, the O_{ads} was consumed and the peak of $C^{18}O_2$ almost disappeared, while $C^{16}O_2$ was still detected, which confirmed that O_{latt} was activated and continuously involved in toluene oxidation under illumination. Notably, there was no detectable peak of $C^{16}O^{18}O$, suggesting that the O_{ads} might preferentially oxidize toluene over the replenishment of O_{latt} in absence of O_2.

3.5. Reaction mechanism

It is well known that the ring-opening process is the rate-determining step of toluene oxidation. Thus, clarifying the ring-opening step of toluene is the highlight of exploring the plausible mechanism. Many studies have proposed that the reaction begins from the oxidation of methyl groups and follow the path of toluene → benzyl alcohol → benzaldehyde → benzoic acid [58]. To confirm this inference, the stepwise energy barriers of these intermediates on $LaMnO_3$ and $La_{0.9}Fe_{0.1}MnO_3$ were calculated (Fig. S12). Obviously, the conversion of toluene to benzoic acid exhibited a significant heat release trend on samples, suggesting that toluene was more preferentially converted to benzoic acid. In addition, the toluene conversion over $La_{0.9}Fe_{0.1}MnO_3$ was much more thermodynamically favorable than $LaMnO_3$, which accounted for the higher activity of $La_{0.9}Fe_{0.1}MnO_3$.

Based on the results of in situ DRIFT, $^{18}O_2$ isotope tracing experiment, and DFT calculations, the reaction mechanism in absence of O_2 and in presence of O_2 is presumed and presented in Fig. 9b. Toluene is first adsorbed onto the catalyst by reacting with the reactive oxygen species via the C−H bond of the methyl group to form an intermediate (C_6H_5 −CH_2 −O). In absence of O_2, the catalyst gives up its O_{latt} to oxidize toluene to benzaldehyde directly, and further transform to

benzoic acid and maleic anhydride. Meanwhile, the active components (Mn^{4+} and Fe^{3+}) are reduced, and new surface oxygen vacancies are produced. Since the lack of O_2, the produced oxygen vacancies can be replenished by the movement of O_{latt} from the catalyst bulk, thus enabling the whole reaction cycle to proceed. The enhanced reducibility by Fe doping and the activated O_{latt} by photoactivation significantly promote this process. It showed a typical MvK mechanism. In presence of O_2, the adsorbed toluene follows the rapid dehydrogenation step as benzyl alcohol, benzaldehyde, and benzoic acid. The initiated benzoate then proceeds through a ring-opening step to form maleic anhydride, which is further oxidized and finally CO_2 and H_2O [51]. Notably, the oxygen vacancies formed during the oxidation under oxygen-rich conditions can be more readily replenished by gaseous O_2 rather than bulk O_{latt} due to the easier activation of gaseous O_2 on the catalyst surface [43]. And there are other active electrophilic oxygen species (e.g., O_2^-, O^-) formed in presence of O_2 [59]. Since the nature of reactive oxygen species strongly influences product selectivity [60], it differs from that of absence of O_2, the adsorbed toluene is firstly oxidized to benzyl alcohol.

3.6. The co-effect of Fe doping and photoactivation for reactions

In this work, Fe doping is demonstrated to improve the mobility and amount of surface O_{latt} species, as well as low-temperature reducibility by XPS, O_2-TPD and H_2-TPR characterizations, while the photoactivation effect has also been shown to be effective in activating surface O_{latt} species by CO-TPR, in situ DRIFT, $^{18}O_2$ isotope tracing experiment and DFT calculations. The two have synergistically promoted the oxidation of toluene. From the perspective of practical applications, in addition to activity, we also investigated the co-effect of Fe doping and photoactivation on other aspects, such as resistance and durability.

3.6.1. The resistance to complex gas components

O_2 is indispensable in catalytic reactions. However, O_2 concentration may vary from field to field in the actual exhaust gas, it is meaningful to examine the effect of varying O_2 concentrations on the catalytic activity. To explore the impact of photoactivation more scientifically, we set the temperature of TCO to 208 °C, in which the activity is close to that of PTCO. As displayed in Fig. 10a, with the O_2 concentration dropped to 6%, the samples under PTCO reaction showed only a slight decrease, whereas the performance of $La_{0.9}Fe_{0.1}MnO_3$-TCO was inhibited (from 87.7% to 74.9%). Interestingly, we found there were more intermediates deposited on used-$La_{0.9}Fe_{0.1}MnO_3$-TCO via FTIR analysis, which could mask active sites thus resulting in the decrease of activity (Fig. S13 and Text S5). While the light activated more O_{latt} species to participate in the deep oxidation of toluene, which reduced the accumulation of intermediates and exposed more active sites, enabling the activity to be
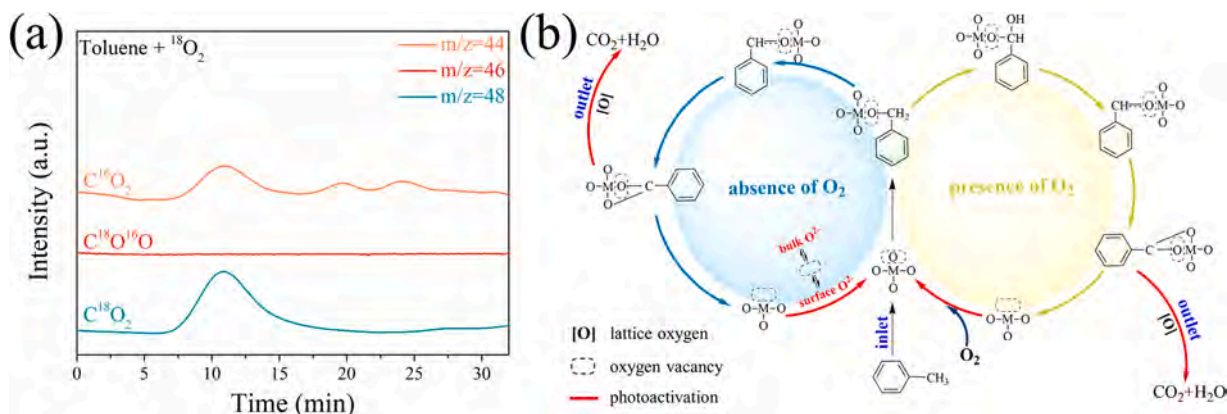

Fig. 9. (a) MS results of evolution of CO_2 in $^{18}O_2$ isotope tracing experiment over $La_{0.9}Fe_{0.1}MnO_3$ under illumination. (b) The plausible pathways and mechanisms of toluene oxidation in absence of O_2 and in presence of O_2.
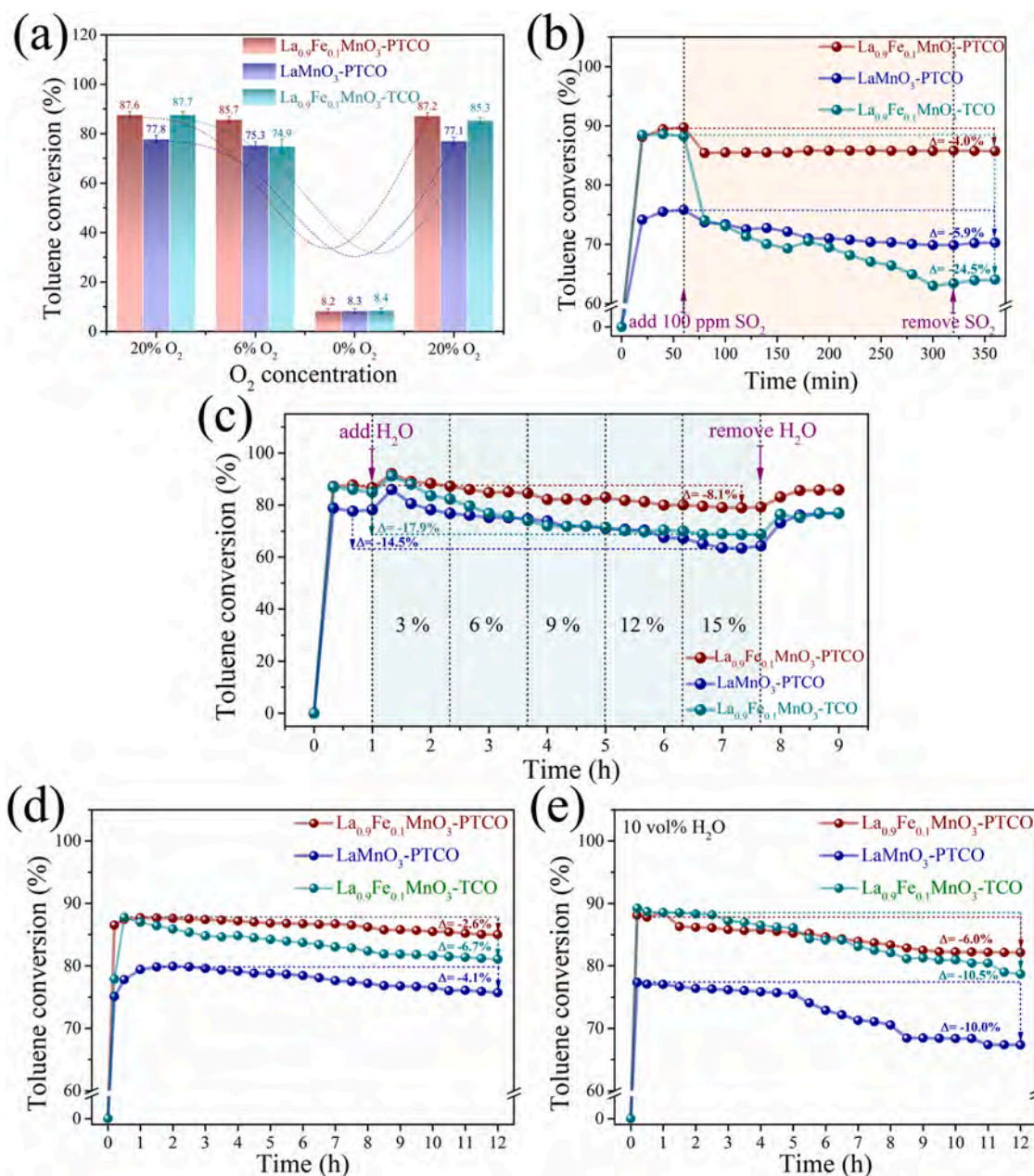
Fig. 10. Effect of (a) O_2 concentration, (b) SO_2 and (c) water vapor on toluene conversion. of $La_{0.9}Fe_{0.1}MnO_3$-PTCO, $LaMnO_3$-PTCO, and $La_{0.9}Fe_{0.1}MnO_3$-TCO. The comparative durability experiments (d) in absence and (e) in presence of water vapor. (PTCO reaction condition: 500 ppm toluene, 20 vol% O_2/N_2, light intensity=1.3×10^4 W/m^2; TCO reaction condition: 500 ppm toluene, 20 vol% O_2/N_2, 208 °C).

maintained. Additionally, in the absence of O_2, all samples exhibited relatively low activity, while they were recovered as the O_2 concentration increased again to 20%. Notably, the $La_{0.9}Fe_{0.1}MnO_3$ still achieved 87.2% toluene conversion at 6 vol% O_2 under illumination, illustrating its practical applicability in low O_2 conditions, such as coal flue gas.

In general, industrial exhaust contains various components, such as SO_2 and H_2O. Thereby, we investigated the resistance of the samples to SO_2 and H_2O. After introducing 100 ppm SO_2 into the reaction system, the toluene conversion of all samples showed a significant and irreversible decrease (Fig. 10b). Such a negative effect may be attributed to the cumulative adsorption of SO_2 and the formation of sulfur/sulfate deposition at active sites [61]. Thereinto, the $La_{0.9}Fe_{0.1}MnO_3$-TCO activity ($\Delta=-24.5\%$) dropped more dramatically than that of $La_{0.9}Fe_{0.1}MnO_3$-PTCO ($\Delta=-4.0\%$) and $LaMnO_3$-PTCO ($\Delta=-5.9\%$). It implies that Fe doping and photoactivation can improve the resistance of the catalyst to SO_2 to some extent, where photoactivation contributes

more. Instead of SO_2, the deactivation induced by H_2O is reversible. As displayed in Fig. 10c, with continuously increasing the H_2O concentrations, the toluene conversion exhibited a transient increase and then a slow decrease in all samples. After cutting off H_2O, the activity of all samples was reversible. The transient increase of activity is probably due to the activation effect of H_2O on surface adsorbed oxygen species (O_2^-, O_2^{2-} etc.), which reacted according to the equation: O_2^-, $O_2^{2-} + H_2O \rightarrow$ 2 $O^* + 2 -OH$ [62]. This may favor the adsorption and activation of toluene, however, as the H_2O concentration increases from 3 to 15 vol%, the excess H_2O molecules will competitively occupy the active sites and continue to accumulate, which results in a continuous decrease in activity. In contrast, the $La_{0.9}Fe_{0.1}MnO_3$-PTCO exhibited more superior H_2O resistance with only a slight decrease of 8.1%, whereas that of $LaMnO_3$-PTCO and $La_{0.9}Fe_{0.1}MnO_3$-TCO decreased 14.5% and 17.9%, respectively. In other words, Fe doping and photoactivation effect

synergistically improve the resistance to H_2O.

3.6.2. *The durability*

As mentioned in Section 3.1, the $La_{0.9}Fe_{0.1}MnO_3$ exhibited outstanding durability in a 34 h toluene stream. To clarify the effect of Fe doping and photoactivation on durability, a comparative experiment with 12 h toluene flow was conducted in presence or in absence of water vapor. As shown in Fig. 10d and e, in absence of water vapor, the activity of all samples had varying decreases as the sequence of $La_{0.9}Fe_{0.1}MnO_3$-PTCO ($\Delta=-2.6\%$) < $LaMnO_3$-PTCO ($\Delta=-4.1\%$) < $La_{0.9}Fe_{0.1}MnO_3$-TCO ($\Delta=-6.7\%$). And the crystal phase structure of $La_{0.9}Fe_{0.1}MnO_3$ could be well maintained after reactions (Fig. S14). Likewise, the activity of samples followed the same order in presence of water vapor (10 vol% H_2O): $La_{0.9}Fe_{0.1}MnO_3$-PTCO ($\Delta=-6.0\%$) < $LaMnO_3$-PTCO ($\Delta=-10.0\%$) < $La_{0.9}Fe_{0.1}MnO_3$-TCO ($\Delta=-10.5\%$). It is clear that Fe doping and photoactivation synergistically improve the durability.

4. Conclusion

In conclusion, the $La_{1-x}Fe_xMnO_3$ ($0 \leq x \leq 0.2$) samples were synthesized successfully via citrate sol-gel method. Under full spectrum illumination of 1.3×10^4 W/m², $La_{0.9}Fe_{0.1}MnO_3$ exhibited a more superior activity (86.7% toluene conversion and 84.6% CO_2 yield) for toluene oxidation. Through controlled experiments, it was unraveled that the photothermal activity mainly derived from light-driven heat. The results show that the Fe doping and photoactivation synergistically improve the PTCO performance for toluene. Specifically, the doping of Fe not only promotes the formation/regeneration of reactive oxygen species, but improves the mobility and quantity of surface O_{latt}, as well as the low-temperature reducibility; whereas the light supplies the heat energy for the reaction and significantly contributes to the activation of O_{latt} species. Therefore, the co-effect of Fe doping and photoactivation could enhance the PTCO activity, selectivity, resistance to complex gas components, and durability. Moreover, the plausible pathways and mechanisms of toluene oxidation were suggested as adsorbed toluene → benzyl alcohol (in presence of O_2) → benzaldehyde → benzoic acid → maleic anhydride → CO_2 + H_2O. This work opens a new perspective on $LaMnO_3$-based photothermal catalysts with full spectrum response for VOCs degradation.

CRediT authorship contribution statement

Qi Yu: Conceptualization, Methodology, Data analysis, Investigation, Writing – review & editing. **Caiting Li:** Resources, Supervision, Data curation. **Jungang Zhao:** Methodology, Writing – review & editing, Validation. **Xuan Liu:** Resources, Writing – review & editing, Supervision. **Le Huang:** Writing – review & editing. **Youcai Zhu:** Writing–review & editing. **Kuang Yang:** Writing–review & editing. **Ziang Zhang:** Writing – review & editing. **Dengsheng Ma:** Software, Writing – review & editing. **Ying Zhang:** Visualization, Writing – review & editing. **Qi Huang:** Writing – review & editing.

Declaration of Competing Interest

The authors declare that they have no known competing financial interests or personal relationships that could have appeared to influence the work reported in this paper.

Data Availability

Data will be made available on request.

Acknowledgements

Appendix A. Supporting information

References

[1] Y. Liu, J. Deng, S. Xie, Z. Wang, H. Dai, Catalytic removal of volatile organic compounds using ordered porous transition metal oxide and supported noble metal catalysts, Chin. J. Catal. 37 (2016) 1193–1205.

[2] L. Aidaoui, A.G. Triantafyllou, A. Azzi, S.K. Garas, V.N. Matthaios, Elevated stacks' pollutants' dispersion and its contributions to photochemical smog formation in a heavily industrialized area, Air Qual. Atmos. Health 8 (2015) 213–227.

[3] L. Tan, J. Zhu, X. He, M. Zhou, S. Zhang, The mechanism of toluene absorption by phosphonium ionic liquids with multiple sites, J. Mol. Liq. 331 (2021) 115501.

[4] T. Shou, Y. Li, M.T. Bernards, C. Becco, G. Cao, Y. Shi, Y. He, Degradation of gas-phase o-xylene via combined non-thermal plasma and Fe doped LaMnO3 catalysts: byproduct control, J. Hazard. Mater. 387 (2020) 121750.

[5] Q. Yu, C. Li, D. Ma, J. Zhao, X. Liu, C. Liang, Y. Zhu, Z. Zhang, K. Yang, Layered double hydroxides-based materials as novel catalysts for gaseous VOCs abatement: Recent advances and mechanisms, Coord. Chem. Rev. 471 (2022), 214738.

[6] F. Wang, J. Deng, S. Impeng, Y. Shen, T. Yan, G. Chen, L. Shi, D. Zhang, Unraveling the effects of the coordination number of Mn over α-MnO2 catalysts for toluene oxidation, Chem. Eng. J. 396 (2020), 125192.

[7] W. Qu, P. Wang, M. Gao, J.-Y. Hasegawa, Z. Shen, Q. Wang, R. Li, D. Zhang, Delocalization effect promoted the indoor air purification via directly unlocking the ring-opening pathway of toluene, Environ. Sci. Technol. 54 (2020) 9693–9701.

[8] Y. Shen, J. Deng, L. Han, W. Ren, D. Zhang, Low-temperature combustion of toluene over Cu-doped SmMn2O5 mullite catalysts via creating highly active Cu2+–O–Mn4+ Sites, Environ. Sci. Technol. 56 (2022) 10433–10441.

[9] Y. Li, S. Wu, J. Wu, Q. Hu, C. Zhou, Photothermocatalysis for efficient abatement of CO and VOCs, J. Mater. Chem. A 8 (2020) 8171–8194.

[10] Y. Yang, S. Zhao, L. Cui, F. Bi, Y. Zhang, N. Liu, Y. Wang, F. Liu, C. He, X. Zhang, Recent advancement and future challenges of photothermal catalysis for VOCs elimination: From catalyst design to applications, Green. Energy Environ. (2022).

[11] C. Liang, C. Li, Y. Zhu, X. Du, Y. Zeng, Y. Zhou, J. Zhao, S. Li, X. Liu, Q. Yu, Y. Zhai, Light-driven photothermal catalysis for degradation of toluene on CuO/TiO2 Composite: Dominating photocatalysis and auxiliary thermalcatalysis, Appl. Surf. Sci. 601 (2022), 154144.

[12] R. Ma, J. Sun, D.H. Li, J.J. Wei, Review of synergistic photo-thermo-catalysis: Mechanisms, materials and applications, Int. J. Hydrog. Energy 45 (2020) 30288–30324.

[13] C. Zhou, L. Cheng, Y. Li, M. Zeng, Y. Yang, J. Wu, X. Zhao, Novel photoactivation promotes catalytic abatement of CO on CuO mesoporous nanosheets with full solar spectrum illumination, Appl. Catal. B-Environ. 225 (2018) 314–323.

[14] J. Kong, C. Jiang, Z. Rui, S. Liu, F. Xian, W. Ji, H. Ji, Photothermocatalytic synergistic oxidation: an effective way to overcome the negative water effect on supported noble metal catalysts for VOCs oxidation, Chem. Eng. J. 397 (2020), 125485.

[15] J. Kong, Z. Xiang, G. Li, T. An, Introduce oxygen vacancies into CeO2 catalyst for enhanced coke resistance during photothermocatalytic oxidation of typical VOCs, Appl. Catal. B-Environ. 269 (2020), 118755.

[16] J.-J. Li, S.-C. Cai, E.-Q. Yu, B. Weng, X. Chen, J. Chen, H.-P. Jia, Y.-J. Xu, Efficient infrared light promoted degradation of volatile organic compounds over photo-thermal responsive Pt-rGO-TiO2 composites, Appl. Catal. B-Environ. 233 (2018) 260–271.

[17] J.-J. Li, E.-Q. Yu, S.-C. Cai, X. Chen, J. Chen, H.-P. Jia, Y.-J. Xu, Noble metal free, CeO2/LaMnO3 hybrid achieving efficient photo-thermal catalytic decomposition of volatile organic compounds under IR light, Appl. Catal. B-Environ. 240 (2019) 141–152.

[18] E. Yu, J. Chen, H. Jia, Enhanced light-driven photothermocatalytic activity on selectively dissolved LaTi1−xMnxO3+δ perovskites by photoactivation, J. Hazard. Mater. 399 (2020), 122942.

[19] J. Chen, Z. He, G. Li, T. An, H. Shi, Y. Li, Visible-light-enhanced photothermocatalytic activity of ABO3-type perovskites for the decontamination of gaseous styrene, Appl. Catal. B-Environ. 209 (2017) 146–154.

[20] Y. Zheng, W. Wang, D. Jiang, L. Zhang, Amorphous MnOx modified Co3O4 for formaldehyde oxidation: improved low-temperature catalytic and photothermocatalytic activity, Chem. Eng. J. 284 (2016) 21–27.

[21] P. Kanhere, Z. Chen, A review on visible light active perovskite-based photocatalysts, Molecules (2014) 19995–20022.

[22] W. Si, W. Wang, Y. Peng, J. Li, Selective dissolution of A-site cations in ABO3 perovskites: a new path to high-performance catalysts, Angew. Chem. Int. Ed. 54 (2015) 7954–7957.

[23] W. Yang, R. Zhang, B. Chen, N. Bion, D. Duprez, S. Royer, Activity of perovskite-type mixed oxides for the low-temperature CO oxidation: evidence of oxygen species participation from the solid, J. Catal. 295 (2012) 45–58.

[24] Y. Xu, J. Dhainaut, J.-P. Dacquin, A.-S. Mamede, M. Marinova, J.-F. Lamonier, H. Vezin, H. Zhang, S. Royer, La1-x(Sr, Na, K)xMnO3 perovskites for HCHO oxidation: the role of oxygen species on the catalytic mechanism, Appl. Catal. B Environ. 287 (2021) 119955.

[25] L. Zhao, L. Jiang, Y. Huang, J. Zhang, J. Tang, C. Li, Mechanism investigation of three-dimensional porous A-site substituted La1-xCoxFeO3 catalysts for simultaneous oxidation of NO and toluene with H2O, Appl. Surf. Sci. 578 (2022), 151977.

[26] M. Wang, T. Zhao, X. Dong, M. Li, H. Wang, Effects of Ce substitution at the A-site of LaNi0.5Fe0.5O3 perovskite on the enhanced catalytic activity for dry reforming of methane, Appl. Catal. B-Environ. 224 (2018) 214–221.

[27] Y. Wang, Y. Zheng, Y. Wang, H. Wang, X. Zhu, Y. Wei, Y. Wang, L. Jiang, Z. Yang, K. Li, Evaluation of Fe substitution in perovskite LaMnO3 for the production of high purity syngas and hydrogen, J. Power Sources 449 (2020), 227505.

[28] B. Song, C. Li, X. Du, S. Li, Y. Zhang, Y. Lyu, Q. Zhou, Superior performance of Cu-Ce binary oxides for toluene catalytic oxidation: Cu-Ce synergistic effect and reaction pathways, Fuel 306 (2021), 121654.

[29] E. Yu, J. Li, J. Chen, J. Chen, Z. Hong, H. Jia, Enhanced photothermal catalytic degradation of toluene by loading Pt nanoparticles on manganese oxide: Photoactivation of lattice oxygen, J. Hazard. Mater. 388 (2020), 121800.

[30] J. Chen, X. Chen, W. Xu, Z. Xu, J. Chen, H. Jia, J. Chen, Hydrolysis driving redox reaction to synthesize Mn-Fe binary oxides as highly active catalysts for the removal of toluene, Chem. Eng. J. 330 (2017) 281–293.

[31] C. Zhang, Y. Guo, Y. Guo, G. Lu, A. Boreave, L. Retailleau, A. Baylet, A. Giroir-Fendler, LaMnO3 perovskite oxides prepared by different methods for catalytic oxidation of toluene, Appl. Catal. B-Environ. 148–149 (2014) 490–498.

[32] N.E. Machin, C. Karakaya, A. Celepci, Catalytic combustion of methane on La-, Ce-, and Co-based mixed oxides, Energy Fuel. 22 (2008) 2166–2171.

[33] C. Zhang, C. Wang, W. Zhan, Y. Guo, Y. Guo, G. Lu, A. Baylet, A. Giroir-Fendler, Catalytic oxidation of vinyl chloride emission over LaMnO3 and LaB0.2Mn0.8O3 (B▭Co, Ni, Fe) catalysts, Appl. Catal. B Environ. 129 (2013) 509–516.

[34] X. Zhao, Q. Yang, J. Cui, XPS study of surface absorbed oxygen of ABO3 mixed oxides, J. Rare Earth. 26 (2008) 511–514.

[35] W. Tang, X. Wu, D. Li, Z. Wang, G. Liu, H. Liu, Y. Chen, Oxalate route for promoting activity of manganese oxide catalysts in total VOCs' oxidation: effect of calcination temperature and preparation method, J. Mater. Chem. A 2 (2014) 2544–2554.

[36] M. Romero-Sáez, D. Divakar, A. Aranzabal, J.R. González-Velasco, J.A. González-Marcos, Catalytic oxidation of trichloroethylene over Fe-ZSM-5: Influence of the preparation method on the iron species and the catalytic behavior, Appl. Catal. B-Environ. 180 (2016) 210–218.

[37] C. Ge, Y. Yu, D. An, Q. Tong, C. Tang, F. Gao, J. Sun, L. Dong, Surface configuration modulation in FeOx-CeO2/γ-Al2O3 catalysts and its influence in CO oxidation, J. Catal. 386 (2020) 139–146.

[38] Y. Wang, J. Wu, G. Wang, D. Yang, T. Ishihara, L. Guo, Oxygen vacancy engineering in Fe doped akhtenskite-type MnO2 for low-temperature toluene oxidation, Appl. Catal. B-Environ. 285 (2021), 119873.

[39] X. Liu, J. Mi, L. Shi, H. Liu, J. Liu, Y. Ding, J. Shi, M. He, Z. Wang, S. Xiong, Q. Zhang, Y. Liu, Z.-S. Wu, J. Chen, J. Li, In situ modulation of a-site vacancies in LaMnO3.15 perovskite for surface lattice oxygen activation and boosted redox reactions, Angew. Chem. Int. Ed. 60 (2021) 26747–26754.

[40] Y.P. Wang, L. Zhou, M.F. Zhang, X.Y. Chen, J.M. Liu, Z.G. Liu, Room-temperature saturated ferroelectric polarization in BiFeO3 ceramics synthesized by rapid liquid phase sintering, Appl. Phys. Lett. 84 (2004) 1731–1733.

[41] L. Liu, J. Sun, J. Ding, Y. Zhang, T. Sun, J. Jia, Highly active Mn3−xFexO4 spinel with defects for toluene mineralization: insights into regulation of the oxygen vacancy and active metals, Inorg. Chem. 58 (2019) 13241–13249.

[42] S. Mo, Q. Zhang, J. Li, Y. Sun, Q. Ren, S. Zou, Q. Zhang, J. Lu, M. Fu, D. Mo, J. Wu, H. Huang, D. Ye, Highly efficient mesoporous MnO2 catalysts for the total toluene oxidation: Oxygen-Vacancy defect engineering and involved intermediates using in situ DRIFTS, Appl. Catal. B-Environ. 264 (2020) 118464.

[43] H. Sun, Z. Liu, S. Chen, X. Quan, The role of lattice oxygen on the activity and selectivity of the OMS-2 catalyst for the total oxidation of toluene, Chem. Eng. J. 270 (2015) 58–65.

[44] Y. Liu, H. Dai, J. Deng, Y. Du, X. Li, Z. Zhao, Y. Wang, B. Gao, H. Yang, G. Guo, In situ poly(methyl methacrylate)-templating generation and excellent catalytic performance of MnOx/3DOM LaMnO3 for the combustion of toluene and methanol, Appl. Catal. B-Environ. 140–141 (2013) 493–505.

[45] L. Liu, J. Li, H. Zhang, L. Li, P. Zhou, X. Meng, M. Guo, J. Jia, T. Sun, In situ fabrication of highly active γ-MnO2/SmMnO3 catalyst for deep catalytic oxidation of gaseous benzene, ethylbenzene, toluene, and o-xylene, J. Hazard. Mater. 362 (2019) 178–186.

[46] X. Lin, S. Li, H. He, Z. Wu, J. Wu, L. Chen, D. Ye, M. Fu, Evolution of oxygen vacancies in MnOx-CeO2 mixed oxides for soot oxidation, Appl. Catal. B-Environ. 223 (2018) 91–102.

[47] Y. Feng, C. Wang, C. Wang, H. Huang, H.-C. Hsi, E. Duan, Y. Liu, G. Guo, H. Dai, J. Deng, Catalytic stability enhancement for pollutant removal via balancing lattice oxygen mobility and VOCs adsorption, J. Hazard. Mater. 424 (2022), 127337.

[48] M. Zeng, Y. Li, M. Mao, J. Bai, L. Ren, X. Zhao, Synergetic effect between photocatalysis on TiO2 and thermocatalysis on CeO2 for gas-phase oxidation of benzene on TiO2/CeO2 nanocomposites, ACS Catal. 5 (2015) 3278–3286.

[49] Y.-K. Hsu, Y.-C. Chen, Y.-G. Lin, L.-C. Chen, K.-H. Chen, Birnessite-type manganese oxides nanosheets with hole acceptor assisted photoelectrochemical activity in response to visible light, J. Mater. Chem. 22 (2012) 2733–2739.

[50] Y. Yang, Y. Li, M. Mao, M. Zeng, X. Zhao, UV–visible–infrared light driven thermocatalysis for environmental purification on ramsdellite MnO2 hollow spheres considerably promoted by a novel photoactivation, ACS Appl. Mater. Inter. 9 (2017) 2350–2357.

[51] G. Gao, Y. Liao, W. Li, Z. Li, H. Xu, W. Huang, N. Yan, L. Fan, Z. Qu, Active surface RuOx species originating from size-driving self-dispersion process for toluene catalytic combustion, Chem. Eng. J. 441 (2022), 136127.

[52] Z. Su, W. Yang, C. Wang, S. Xiong, X. Cao, Y. Peng, W. Si, Y. Weng, M. Xue, J. Li, Roles of oxygen vacancies in the bulk and surface of CeO2 for toluene catalytic combustion, Environ. Sci. Technol. 54 (2020) 12684–12692.

[53] Y. Zhang, A. Martin, H. Berndt, B. Lücke, M. Meisel, FTIR investigation of surface intermediates formed during the ammoxidation of toluene over vanadyl pyrophosphate, J. Mol. Catal. A: Chem. 118 (1997) 205–214.

[54] Z. Chen, Y. Peng, J. Chen, C. Wang, H. Yin, H. Wang, C. You, J. Li, Performance and mechanism of photocatalytic toluene degradation and catalyst regeneration by thermal/UV treatment, Environ. Sci. Technol. 54 (2020) 14465–14473.

[55] J. Zhong, Y. Zeng, D. Chen, S. Mo, M. Zhang, M. Fu, J. Wu, Z. Su, P. Chen, D. Ye, Toluene oxidation over Co3+-rich spinel Co3O4: evaluation of chemical and by-product species identified by in situ DRIFTS combined with PTR-TOF-MS, J. Hazard. Mater. 386 (2020), 121957.

[56] Y. Shen, J. Deng, S. Impeng, S. Li, T. Yan, J. Zhang, L. Shi, D. Zhang, Boosting toluene combustion by engineering Co–O strength in cobalt oxide catalysts, Environ. Sci. Technol. 54 (2020) 10342–10350.

[57] K. Li, J. Chen, B. Bai, S. Zhao, F. Hu, J. Li, Bridging the reaction route of toluene total oxidation and the structure of ordered mesoporous Co3O4: the roles of surface sodium and adsorbed oxygen, Catal. Today 297 (2017) 173–181.

[58] J. He, L. Chen, D. Ding, Y.-K. Yang, C.-T. Au, S.-F. Yin, Facile fabrication of novel Cd3(C3N3S3)2/CdS porous composites and their photocatalytic performance for toluene selective oxidation under visible light irradiation, Appl. Catal. B-Environ. 233 (2018) 243–249.

[59] F. Arena, G. Trunfio, J. Negro, B. Fazio, L. Spadaro, Basic evidence of the molecular dispersion of MnCeOx catalysts synthesized via a novel "redox-precipitation" route, Chem. Mater. 19 (2007) 2269–2276.

[60] A.R. Gandhe, J.S. Rebello, J.L. Figueiredo, J.B. Fernandes, Manganese oxide OMS-2 as an effective catalyst for total oxidation of ethyl acetate, Appl. Catal. B-Environ. 72 (2007) 129–135.

[61] Z. Wang, S. Xie, Y. Feng, P. Ma, K. Zheng, E. Duan, Y. Liu, H. Dai, J. Deng, Simulated solar light driven photothermal catalytic purification of toluene over iron oxide supported single atom Pt catalyst, Appl. Catal. B-Environ. 298 (2021), 120612.

[62] X. Du, C. Li, L. Zhao, J. Zhang, L. Gao, J. Sheng, Y. Yi, J. Chen, G. Zeng, Promotional removal of HCHO from simulated flue gas over Mn-Fe oxides modified activated coke, Appl. Catal. B-Environ. 232 (2018) 37–48.